Volume 1 | Number 1 | Jan 2013 | Pages 1–100

PCCP

Physical Chemistry Chemical Physics
www.rsc.org/pccp

ROYAL SOCIETY OF CHEMISTRY

ROYAL SOCIETY OF CHEMISTRY

www.rsc.org/pccp

PAPER

Preparation of Water-Dispersible Porous g-C$_3$N$_4$ with Improved Photocatalytic Activity by Chemical Oxidation

Hui-Jun Li,[a] Bo-Wen Sun,[a] Li Sui,[b] Dong-Jin Qian[a] and Meng Chen[*a]

Hydrophilic treatment of the bulk graphene-like carbon nitride (g-C$_3$N$_4$) for future applications has aroused extensive interest, due to their enhanced specific surface area and unusual electronic property. Herein, water- dispersible g-C$_3$N$_4$ with a porous structure can be obtained by chemical oxidation of the bulk g-C$_3$N$_4$ with K$_2$Cr$_2$O$_7$/H$_2$SO$_4$. Acid oxidation results in the production of hydroxyl and carboxyl groups to its basal plane, and the formation of porous structure of the g-C$_3$N$_4$ at the same time. The porous g-C$_3$N$_4$ appears as networks with tens of micrometers in width and possesses a high specific surface area of 235.2 m^2 g^{-1}. The final concentration of the porous g-C$_3$N$_4$ can be up to 3 mg mL^{-1}. Compared with the bulk g-C$_3$N$_4$, the as-obtained porous g-C$_3$N$_4$ exhibits excellent water dispersion stability and shows great superiority in photoinduced charge carrier separation and transfer. The photocatalytic activities towards organic pollutants degradation of the porous g-C$_3$N$_4$ are much higher than those of the bulk due to the larger band gap (by 0.2 eV) and specific surface areas.

1. Introduction

Global researches on visible-light-active photocatalysts for environmental protection and solar fuels have attracted lots of attention recently.[1] Among the various catalytic materials, graphitic carbon nitride (g-C$_3$N$_4$) is a metal-free photocatalyst with appropriate band edges and a large band gap of 2.70 eV,[2] which can catalyze a number of reactions, such as photodegradation of organic pollutants or photochemical splitting of water.[3, 4] However, the bulk g-C$_3$N$_4$ materials prepared by direct polycondensation from suitable precursors, including melamine, thiourea and guanidine hydrochloride (GndCl), generally have very low surface areas (less than 10 m^2 g^{-1}) and poor photocatalytic activity.[5] Despite the new modification methods, for instance, morphology control,[6] coupling with other materials[7-9] or element doping,[10, 11] the insoluble property of carbon nitrides in common solvents (water, ethanol, acetone and so on) also makes further functionalization inconvenient and limits their applications.

The studies on the structure of g-C$_3$N$_4$ have indicated that there are stronger covalent C-N bonds instead of C-C bonds in each layer. The planar cohesion between strands of polymeric melon units is mainly attributed to hydrogen bonding, which is less strong compared with the covalent bonding cohesion in graphite.[12] Motivated by the liquid-phase exfoliation methods to prepare graphene oxide, researchers have successfully exfoliated the bulk g-C$_3$N$_4$ into water-dispersible C$_3$N$_4$ nanosheets of a high quality. The exfoliation techniques involves intercalation and surface passivation by solvent molecules (H$_2$O,[13] isopropanol,[14] 1,3-butylene glycol,[15] and

H$_2$SO$_4$[16, 17]). Layer materials could adsorb solvent molecules into the spacing between layers. The intercalation of solvents between the layers increases the layer spacing and weakens the interlayer attraction. Subsequent treatment such as sonication or thermal shock can result in exfoliation. If the surface energy of the solvent matches with that of bulk g-C$_3$N$_4$, the energy disparity between aggregated and exfoliated states will be very small. The as-obtained nanosheets are then stabilized as exfoliated dispersion.[18] However, these strategies require a rather long sonication time (10-16 h), and the yield is relatively low (0.15-0.35 mg mL^{-1}). Recently encouraged by the protonation method used to disperse CNTs, Wang et al.[19] firstly reported the reversible protonation of carbon nitride by stirring it with strong mineral acids (37% HCl) for 3 h. The protonation method provides better dispersion in water and a higher surface area. The BET surface area of the pronated g-C$_3$N$_4$ has increased from 8 to 30 m^2 g^{-1}. Then Qiao et al.[20] have prepared proton-functionalized g-C$_3$N$_4$ nanosheets, which exhibit large specific surface area of 305 m^2 g^{-1}.

Although different methods have been developed to produce water-dispersible g-C$_3$N$_4$, the chemical oxidation of bulk g-C$_3$N$_4$ has rarely been reported in literature. As we know, various oxidants have been used to react with carbon nanotubes or graphene in the liquid-phase oxidation methods, including HNO$_3$,[21] HNO$_3$ + H$_2$SO$_4$,[22] KMnO$_4$ + H$_2$SO$_4$,[22] K$_2$Cr$_2$O$_7$ + H$_2$SO$_4$[23, 24] and so on. Treatment with oxidizers results in the production of hydroxyl and carboxyl groups on the basal plane, contributing to water intercalation and its hydrophillicity. The nature of the reactants and oxidants would have a great impact on the degree of oxidation. For example, the widely used Hummers method is not suitable for the exfoliation of g-C$_3$N$_4$.

The strong oxidizing acid, $KMnO_4/H_2SO_4$, is more capable of making ortho hydroxyls[25] and would seriously destroy the planar atomic structure of $g-C_3N_4$, only leading to the formation of carbon nitride based particles.[26] Considering the special structure of $g-C_3N_4$, it is worth anticipating that oxidants with a lower redox potential ($K_2Cr_2O_7/H_2SO_4$) could be used to allow the hydrophilic modification and avoid heavy structure destruction.

Herein, we report a facile method to prepare dispersible $g-C_3N_4$ by chemical oxidation of bulk $g-C_3N_4$ at room temperature. The obtained $g-C_3N_4$ possesses a porous structure with a large surface area (235.2 m^2 g^{-1}) and appears as networks with tens of micrometers in width. Due to the oxygen-containing functional groups on its surface, the final concentration of the $g-C_3N_4$ solution can even be up to 3 mg mL^{-1}. The crystal structure, chemical states and electronic structure of the resultant porous $g-C_3N_4$ have been thoroughly studied. Moreover, the porous $g-C_3N_4$ has an efficient photocatalytic activity towards organic pollutants degradation.

2.   Experimental section

2.1 Synthesis of porous $g-C_3N_4$

$g-C_3N_4$ was prepared by heating dicyandiamide in a muffle furnace at 550 °C for 4 h with a ramp rate of 2.3 °C/min. The porous $g-C_3N_4$ was synthesized via the chemical oxidation of the bulk $g-C_3N_4$ with $K_2Cr_2O_7/H_2SO_4$. 10 g of $K_2Cr_2O_7$ was mixed with 50 mL of H_2SO_4 (98 wt%) in a 100-mL flask and stirred till the solution became brown. 0.5 g of the bulk $g-C_3N_4$ was added into the solution and stirred thoroughly for 2 h at room temperature. Then the mixture was slowly poured into 400 mL of deionized water and cooled to room temperature. After centrifugation at 6000 rpm, the obtained light yellow solid was dialyzed in a dialysis bag to remove all residual acids, and dispersed in water for sonication (1~2 h). Finally, the obtained milk-white suspension was centrifuged at 3000 rpm to remove undispersed $g-C_3N_4$. The supernatant liquid could be supercritical dried for future use.

2.2 Characterization of the samples

The X-ray powder diffraction (XRD) patterns were recorded using a D8 advance X-ray diffractometer (Bruker Company, Germany) in transition mode and Cu K radiation (γ= 1.54056□Å). The X-Ray photoelectron spectroscopy (XPS) was performed on a Kratos Axis Ultra-DLD X-ray photoelectron spectrometer (Shimadzu, Kyoto, Japan). The UV-Vis absorption spectroscopy and room-temperature UV-Vis diffuse reflectance spectroscopy (DRS) were taken at room temperature on a UV-3150 spectrophotometer (Shimadzu, Kyoto, Japan). The photoluminescence (PL) spectroscopy was performed by a RF-5301pc fluorescence spectrometer (Shimadzu, Kyoto, Japan). The Fourier transform infrared (FT-IR) experiment was carried out on a Nicolet Nexus 470 FT-IR spectrometer in the wavenumber range of 400 to 4,000 cm^{-1}. The samples were prepared in the form of pellets together with KBr. Raman spectra were recorded on a SPEX/403 laser Raman spectrometer (JY, France) at room temperature using the 785 nm line of an argon ion laser as the excitation source.

The transmission electron microscope (TEM) images were acquired on a FEI Tecnai G20 field emission electron microscope operating at an accelerating voltage of 200 kV. The field emission scanning electron microscopy (FESEM) images

were taken on an Ultra 55 scanning electron microscope. N_2 and CO_2 adsorption and desorption isotherms were collected on an Autosorb-IQ_2 Quantachrome Instrument at 77 K and 273 K, respectively. Ultra-high purity N_2 and CO_2 (99.995 %) were purchased and used as received. The total pore volumes were estimated from the adsorbed amount at a relative pressure P/P0 of 0.995. The Mott-Schottky experiments were taken on an electrochemical workstation (CHI660D, Shanghai Chenhua, China). The perturbation signal was 20 mV with the frequency at 0.5 kHz.

2.3 Photocatalytic activity

The photocatalytic activities were evaluated by the degradation of RhB in a 100-mL quartz reactor with a circulating water system to maintain a constant temperature. A 300 W Xe lamp (BL-GHX-Xe-300k, Shanghai Bilon) with a 420 nm cutoff filter was used as the light source. In each run, 25 mg of the sample was mixed with 50 mL of RhB solution (10 mg mL^{-1}). Prior to irradiation, the suspension was magnetically stirred in the dark for 100 min to reach the absorption-desorption equilibrium of RhB on the catalyst. The suspension was collected at an interval of 20 min and detected.

3.   Results and discussions

3.1 Mechanism of the Formation of the Porous $g-C_3N_4$

The chemical oxidation method has resulted in the formation of porous structure and hydrophillicity of $g-C_3N_4$ at the same time. The synthetic strategy is illustrated in Fig. 1. Typically, after acid treatment, various hydrophilic functional groups (e.g. –COOH, -OH, -C=O) can be generated at the open ends or defect sites of the bulk $g-C_3N_4$ structure (Fig. 1A).[23, 27] The intercalation and exfoliation of the pristine $g-C_3N_4$ by these oxygen-containing groups could improve the hydrophillicity of $g-C_3N_4$. Then the mixture was slowly poured into water, and the producing heat made the $g-C_3N_4$ immediately expand into large floc floatings, which is poorly dispersible in highly acidic

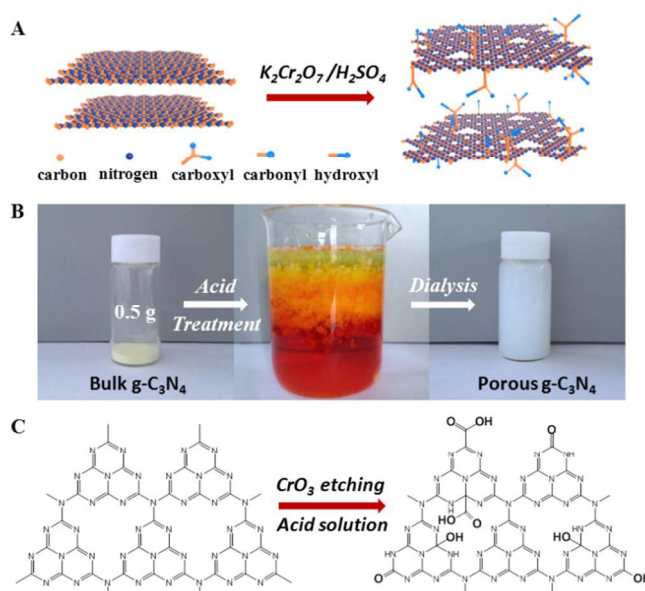**Fig. 1** (A) Schematic illustration, (B) photographs and (C) chemical equation of the chemical-oxidation process from the bulk $g-C_3N_4$ to the porous $g-C_3N_4$ (The hydrogen atoms have not been shown).

solution (Fig. 1B). The rapid heating effect and the following sonication also contribute to the improvement of dispersion.[16] The final concentration of the water-dispersible g-C_3N_4 solution could be up to 3 mg/mL, much higher than that of previously reported g-C_3N_4 nanosheets solution (0.15-0.35 mg mL^{-1}) which was prepared by liquid exfoliation methods.[13-16] The porous g-C_3N_4 solution with a higher concentration appears milky white.

The mechanism of oxidation is based on previous work about the oxidation of carbon nanotubes by $K_2Cr_2O_7/H_2SO_4$.[23, 24] By treating potassium dichromate with sulfuric acid, chromium trioxide (CrO_3) is generated. Then the concentrated H_2SO_4 solution of CrO_3 could effectively etch the surface of pristine g-C_3N_4 and produce hydroxyl groups. The hydroxyl groups may further be converted into a quinone group or break up to O=C-OH groups in the strong oxidative environment (Fig. 1C).[25] It is well known that $K_2Cr_2O_7$ is a milder oxidizing agent than $KMnO_4$. The redox potential of $K_2Cr_2O_7$ is 1.33 eV, and that of $KMnO_4$ is 1.679.[28] Due to the appropriate oxidizing ability of $K_2Cr_2O_7/H_2SO_4$, the slow oxidative etching process could improve the formation of the porous structure, while the two-dimensional (2D) plate-like structure of g-C_3N_4 is still well-preserved.

3.2 Crystal Structure and Chemical States of the Porous g-C_3N_4

The crystal and chemical structure of the porous g-C_3N_4 and the bulk g-C_3N_4 are studied by XRD, XPS, FTIR and Raman spectra. In the XRD patterns presented in Fig. 2A, the low-angle reflection peak at 13.1° stems from the interplanar structural packing motif, such as the hole-to-hole distance.[29] The strong XRD peak (002) of the bulk g-C_3N_4 at around 27.56° originates from the characteristic interlayer stacking reflections like in graphite.[30] With respect to the bulk g-C_3N_4, the (002) peak of the porous g-C_3N_4 is slightly broadened and shifted from 27.56° to 27.91° which indicated a decreased gallery distance between the layers.[26] In our case, the oxidized layers can be planarized by the π-π stacking and hydrogen bonding interactions, which would lead to a denser packing and thus shorten the gallery distance. Moreover, a decrease in the overall intensity can be observed in the porous g-C_3N_4. This change of XRD patterns are similar with that of mesoporous g-C_3N_4 prepared by using SiO_2 nanoparticles or mesoporous SiO_2 as hard templates, which reflects the effect of porous microstructure on the geometic confinement.[31, 32]

Strong evidence of oxygen species in the porous g-C_3N_4 was firstly confirmed by XPS. As shown in Fig. 2B, the profile of bulk g-C_3N_4 does not need to be applied with the Stokes deconvolution method due to its symmetrical nature. The O 1s core level at 532.6 eV is ascribed to the absorbed water[11] and no signal related to the C-O or C=O bond is observed. After acid treatment, line a in Fig. 2B shows a higher density of oxygen-containing species on the porous g-C_3N_4 surface. Also, a slope peak of higher values appears, indicating oxidation-induced acid-bonding characteristics.[24] This main peak could be deconvoluted into four Gaussian-Lorenzian peaks. Three new core levels at 530.7 eV, 531.8 eV and 533.1 eV have been detected, contributed from O=C-OH, C=O and C-OH groups respectively.[33, 34] These signals suggest that the oxygen species are presented not simply as absorbed water but various functional groups on the surface, as a result of the acid treatment of bulk g-C_3N_4. The calculated atomic percentage in the fitting data of C-OH at 533.1 eV is 28.9 %, C=O at 531.8 eV is 36.2% and O=C-OH at 530.7 eV is 16.8%.

The C 1s spectra of the bulk g-C_3N_4 show three peaks located at about 288.0 eV, 286.1 eV and 284.6 eV. The main contribution peak centered at 288.0 eV could be further deconvoluted into two Gaussian-Lorenzian peaks which are originated from sp^2 hybridized carbon bonded to N in C-N-C coordination.[26, 35] The peak at 284.6 eV is typically assigned to graphitic sp^2 C=C bonds, while the lowest peak at 286.1 eV is attributed to the C-NH_2 species.[35] In addition, a new-generated peak at 289.1 eV has been shown in the porous g-C_3N_4, which could be assigned to the COOH species.[36] Meanwhile, the peak in the N 1s spectra can also be deconvoluted into three different peaks at around 398.5 eV, 399.8 eV and 401.1 eV. The peaks are ascribed to sp^2 N atoms in triazine rings (C-N=C), bridging N atoms (N-$(C)_3$) and amino groups carrying hydrogen (C-NH) separately.[2, 14, 36] Another peak at 404.3 eV is due to the charging effect.[2]
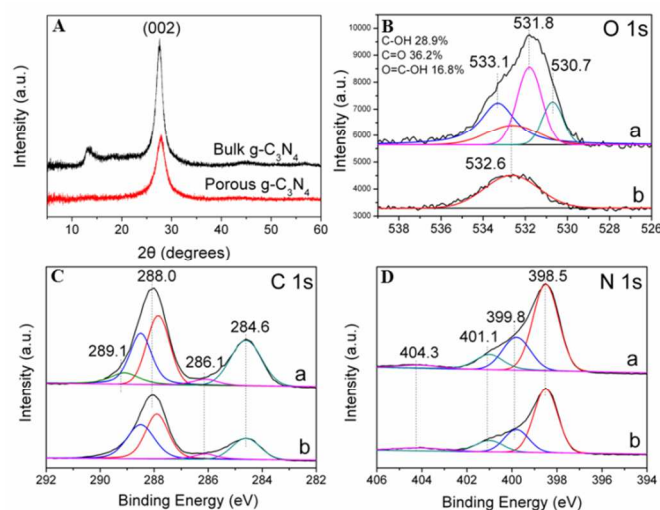

Fig. 2 (A) XRD patterns of the bulk g-C_3N_4 and the porous g-C_3N_4. (B) O 1S, (C) C 1s and (D) N 1s XPS high-resolution spectra of the porous g-C_3N_4 (a) and the bulk g-C_3N_4 (b).

The similar FTIR absorption bands in Fig. S1 indicated that the porous g-C_3N_4 keeps the same chemical structure as the bulk g-C_3N_4. The broad peaks between 3500 and 3000 cm^{-1} can be clearly observed which are caused by the N-H stretches.[37, 38] The peaks between 1800 and 900 cm^{-1} are attributed to s-triazine derivatives such as trigonal C-N(-C)-C or bridging C-NH-C units.[12, 39] The sharp peak at 807 cm^{-1} belongs to the breathing mode of s-triazine ring mode.[40] However, it is difficult to distinguish the C=O or C-O species in the porous g-C_3N_4 by FTIR method. It can be noted that the peaks at 1240 and 1400 cm^{-1} were slightly shifted by 10 cm^{-1} toward high frequencies after oxidation reaction, in the magnified version of FTIR absorption spectra (Fig. 3A). Larkin et al.[41] have once demonstrated that C-O and C-N bonds have similar force constants and could thus lead to their skeletal stretching vibrations in the common IR regions. Liao et al.[42] have shown that the peaks at ca. 1406 cm^{-1}, 1220 cm^{-1} are ascribed to C-O in C-OH and C-O-C functional groups. Other studies have also mentioned that the peaks around 1400 cm^{-1} are attributed to the tertiary C-OH groups stretching,[43, 44] which directly indicates that O-containing species could be located in the same region of aromatic C-N stretching. Therefore, we suspected that the shifts of IR peaks in our work might be caused by the enhanced strength of C-N covalent bonds, which might be resulted from

the electrophilic effect of the oxygen atoms in new C-O bonds adjacent to C-N.

Raman spectroscopy is also used to confirm the presence of oxygen species in the porous samples. A comparison between the bulk g-C_3N_4 and porous g-C_3N_4 has been shown in Fig. 3B. Obviously, the characteristic bands can be observed on both materials[6, 16] while a new broad band at 1257 cm^{-1} has replaced the old peak. According to Lebrun *et al.*'s work,[45, 46] this replacement might be ascribed to the OH in-plane bending mode in C-OH, which further supported our assumptions about the FTIR results.
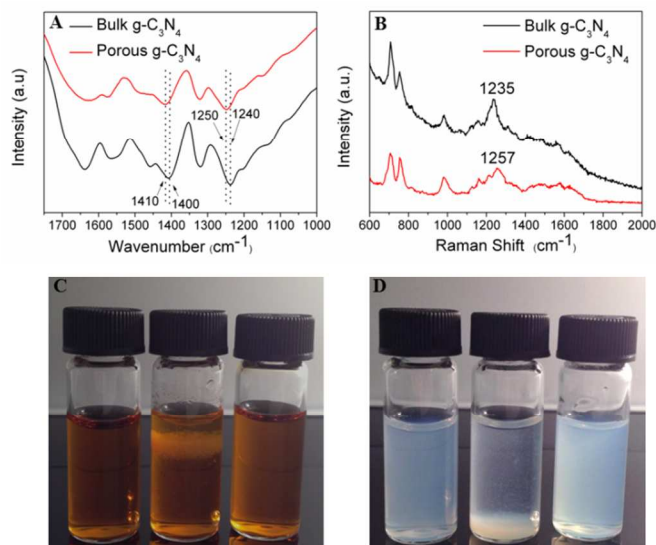

Fig. 3 FTIR spectra (A) and Raman spectra (B) of the bulk g-C_3N_4 and the porous g-C_3N_4. The photograph of identification tests by Fe^{3+} solution (C) and dendrimer solution (D).

To further confirm the oxidation process of the resultant porous g-C_3N_4, several confirmatory experiments have been done as shown in Fig. 3C and 3D. Adding Fe^{3+} or dendrimer aqueous solution directly into the as-prepared porous g-C_3N_4 dispersion has caused obvious floccules. Either coordination of Fe^{3+} with the oxygen-containing functional groups on porous g-C_3N_4, or electrostatic interaction between the protonated amino groups on dendrimer and the oxygen-containing functional groups is assumed to be the driving force for the above phenomenon.[47] Moreover, no floccules appeared when adding Fe^{3+} solution into the water outside the dialysis bag, which excluded the interaction between metal ions and the very few residual acids. Furthermore, the floccules would disappear after injecting an appropriate amount of NaOH solution into the dendrimer-C_3N_4 solutions, which should be owing to the fact that alkali can destroy the electrostatic interaction by releasing these oxygen-containing functional groups. All the results mentioned above could support the oxidation process of the porous g-C_3N_4 with oxidizer.

3.3 Morphology of the Porous g-C_3N_4

The morphology of the porous g-C_3N_4 was investigated with TEM as shown in Fig. 4. The bulk material displays a typical dense and stacked lamellar structure of several micrometers (Fig. 5A, Fig. S2), while the porous g-C_3N_4 was found to have agglomerated into non-uniform networks with tens of micrometers. The formation of networks might be driven by the π-π stacking effect between the layers and hydrogen bonding interactions mediated by the oxygen-containing groups (–COOH, -OH, -C=O).[48] The TEM images with higher magnification have shown that the structure is still graphene-like and a slightly less dense distributed with disordered pores, which is in agreement with the less intense XRD peaks shown in Fig. 2A. The high resolution transmission electron microscopy (HRTEM) has indicated that the etching edges are rather rough. The pores might be caused by the oxidative etching of the melon units on the edge or defect sites of the bulk g-C_3N_4 layers, which is similar to the disordered pores in samples prepared by template methods.[31] Chen *et al.*[11] have also demonstrated that the oxygen-doped g-C_3N_4 appears with hierarchical edges due to the H_2O_2 hydrothermal treatment.

The N_2 adsorption isotherms have shown that the measured surface area of the porous g-C_3N_4 is 235.2 m^2 g^{-1}, which is almost 26 times larger than that of bulk g-C_3N_4 (9.2 m^2 g^{-1}) (Fig. 4E). Their corresponding pore diameter distributions were calculated by BJH method. A centred peak at 10 nm of the porous g-C_3N_4 is observed on the pore-size distribution curve, which should be attributed to the random pores formed by chemical etching. The extended wide peak at 25~100 nm might be owed to the pores in the networks formed by stacking effect. The BET surface area is comparable compared with those mesoporous g-C_3N_4 materials synthesized via the nanocasting methods or g-C_3N_4 nanosheets prepared by exfoliation methods.[5, 15, 16, 31] Besides, the CO_2 adsorption performance at 0 °C was also investigated shown in Fig. 4F. Compared with the bulk samples, the porous g-C_3N_4 presents a higher CO_2 capture capacity of 1.20 mmol g^{-1} at 0 °C. It is reported that the nitrogen-containing groups in mesoporous carbon nitride materials can provide lewis base active sites for absorbing CO_2.[49] In our work, the porous structure in the g-C_3N_4 is beneficial to CO_2 capture capacity due to the capillary
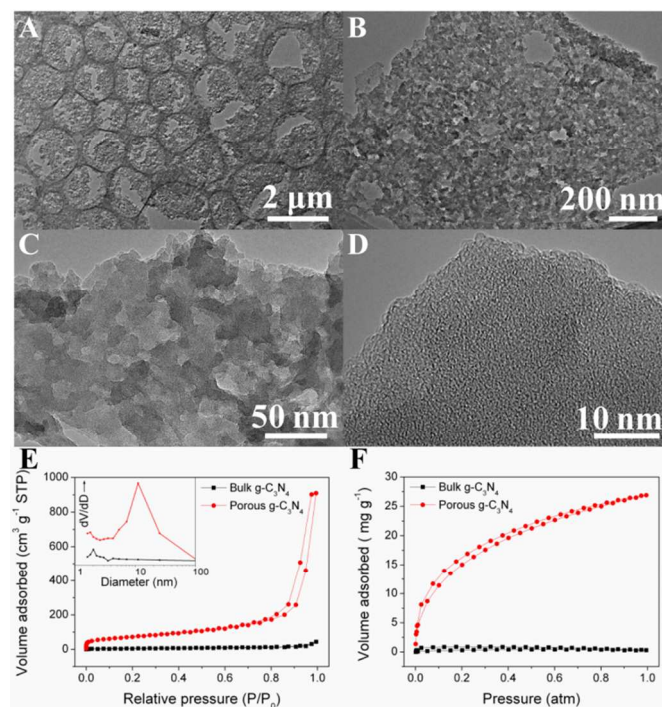

Fig. 4 (A-D) Typical TEM images with different magnification of the as-prepared porous g-C_3N_4 reacting for 2 h. (E) The N_2 and (F) CO_2 adsorption isotherm recorded for the bulk g-C_3N_4 and the porous g-C_3N_4. Inset of (E) is the pore size distribution for the bulk and porous g-C_3N_4.

condensation effect. Besides, owing to the high surface area, more basic sites could be provided, which would improve more CO_2 binding.[50] As a result, the adsorption performance of the porous materials is higher than that of the bulk g-C_3N_4.[49, 51, 52]

In addition, the reaction time is also very important in the formation of porous structures. When the oxidation time of the bulk g-C_3N_4 is extended to 12 h, the obtained products are presented as small patches hanging over the walls of lacey support films shown in Fig. 5B. The planar structure has been seriously destroyed which might be resulted from the defect-consuming step. In this step, the parental graphite-like structure of the carbon nitride was continuously consumed by the oxidation of the already generated defects. Thus, large plates were etched into small patches with irregular morphologies of a size ranging from tens to hundreds of nanometers (shown in Fig. 5).
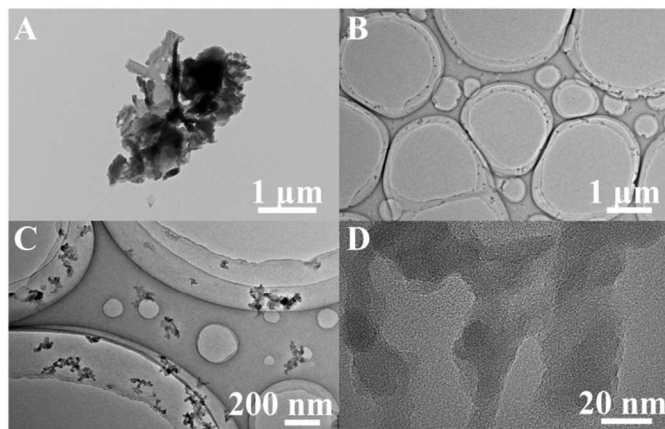

Fig. 5 (A) TEM image of the bulk g-C_3N_4. (B-D) TEM images with different magnification of the as-prepared g-C_3N_4 patches reacting for 12 h.

3.4 Band Structure and Electronic Conductivity of the Porous g-C_3N_4

The electronic and optical properties have been investigated by UV-Vis diffuse reflectance spectroscopy (DRS), Mott-Schottky plots and photoluminescence (PL) (Fig. 6). As can be seen in Fig. 6A, the absorption edge of the porous g-C_3N_4 shows a remarkable blue shift in comparison with the bulk g-C_3N_4. The corresponding bandgaps of the bulk g-C_3N_4 and porous g-C_3N_4 are about 2.54 eV and 2.74 eV, from the inset in Fig. 6A. The blue shift of the absorption edge is in agreement with the color change from yellow of bulk g-C_3N_4 to light yellow of porous g-C_3N_4 (see Fig. S3), since the color of a sample is determined by the absorption spectrum.[53] Aside from the bandgaps, electrochemical Mott-Schottky experiment was performed to determine the relative positions of CB and VB edges. The plots disclose that the porous g-C_3N_4 is a typical n-type semiconductor owing to the positive slope (Fig. 6B).[14, 31, 54] More importantly, the flat band potentials of the bulk and porous g-C_3N_4 were determined to be -1.23 V and -0.88 V versus Hg/Hg_2Cl_2. Combined with the bandgaps obtained from UV-vis DRS curves, the VB level of the porous sample is calculated to be 1.86 V, which is much lowered with a downshift from 1.31 v of the pristine g-C_3N_4 (Fig. 6C). Such optical properties are important for the improvement of photocatalysis.[14, 32] Furthermore, under photoexcitation at 330 nm, the PL spectra of the porous g-C_3N_4 demonstrate that the position of the emission peak is blue shifted by about 33 nm to

435 nm compared with the bulk g-C_3N_4 (Fig. 6D). As shown in the inset of Fig. 6D, the porous g-C_3N_4 emitted blue PL under UV light. The larger band gap and blue shift of PL spectra can be attributed to the strong quantum confinement effect, which are caused by the conduction and valence band shifting in opposite directions and the decrease of conjugation length.[13, 26, 55]
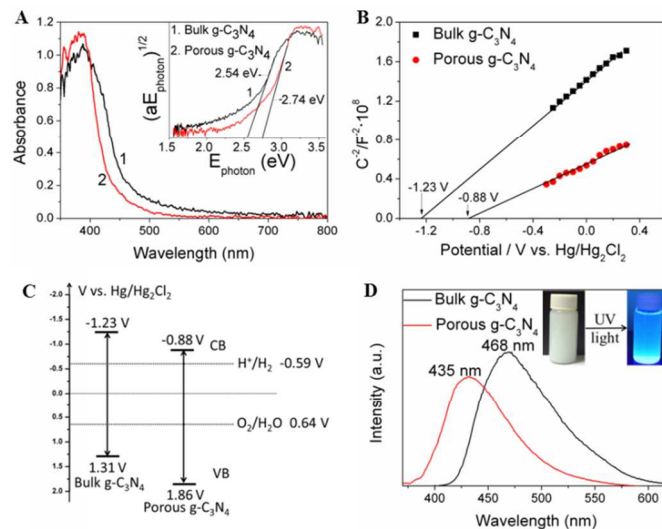

Fig. 6 (A) UV-Visible absorption spectra, (B) Mott-Schottky polt, (C) band structure, and (D) PL spectra of the bulk g-C_3N_4 and the porous g-C_3N_4. Inset of (A) is estimated band gaps of the bulk g-C_3N_4 and the porous g-C_3N_4. Inset of (D) is the color change of the porous g-C_3N_4 solution before and under UV light illumination.

3.5 Photocatalytic Performance

The photocatalytic activities of all the samples were evaluated for RhB photodegradation under visible light irradiation, as is shown in Fig. 7A. After 50 min irradiation with visible light, ca. 31% of RhB is degraded in the presence of bulk g-C_3N_4 while approximately 92% of RhB is decomposed by the porous g-C_3N_4. The photocatalytic degradation efficiency of the porous g-C_3N_4 was enhanced about 61% compared with the bulk g-C_3N_4. The value is also larger than the sulfur-doped mesoporous g-C_3N_4[31] or g-C_3N_4-based composites such as g-C_3N_4-Fe_2O_3.[56] Moreover, it is found that after three successive cycles, the photocatalytic activity of the porous g-C_3N_4 only decreased a little. Therefore, its stability is rather good for further practical applications.

The above results clearly demonstrate that the porous g-C_3N_4 own significantly enhanced photocatalytic activities compared to the bulk g-C_3N_4. As reported before, three steps exist in the semiconductor photocatalysis process, including the photoexciation, the separation and transportation of photoexcited charge carriers, and the photocatalytic reaction. Studies have shown that the synergistic effects of surface area, light absorption and electron transport ability can greatly influence the photocatalytic activity of g-C_3N_4.[2, 3] In our case, more adsorption sites and photocatalytic reaction sites could be provided by the larger Brunauer-Emmett-Teller (BET) specific surface area, during the photocatalysis reaction of the porous g-C_3N_4.[15] On the other hand, the porous structures might contribute to the improvement of photoinduced charge carrier separation and transportation efficiency.[16, 57] More importantly, the larger band gap (0.2 eV) could enhance the conduction

ability of photogenerated electrons due to the quantum confinement effect.[13, 15] As is known, the photoreduction and photooxidation abilities of semiconductors are determined by the potentials of their conduction and valence bands. The positive shift of VB in the porous g-C_3N_4 would make the hole more oxidative and increase its photooxidation ability.[58, 59] Meanwhile, the final potential of the CB is still negative than $2H^+/H_2$ or O_2/O_2^-,[59] indicating that the photogenerated electrons can be trapped by the absorbed O_2 to form into various reactive species (O_2^-, HO_2^-, H_2O_2). This trapping can inhibit the recombination of photoinduced carriers and is crucial for the direct hole oxidation of RhB into CO_2, H_2O, et al.[59, 60]

Moreover, the effect of possible residual $K_2Cr_2O_7/H_2SO_4$ on the degradation of RhB was also investigated (Fig. S4). The theoretical concentration of Cr^{3+} in the 25 mg porous g-C_3N_4 for 50 mL RhB degradation is 0.0023 mg/L. Based on this calculation, we have prepared 50 mL RhB solution containing 0.01 mg/L and 0.005 mg/L Cr^{3+} by using $K_2Cr_2O_7/H_2SO_4$. The degradation result is not good, compared to the porous g-C_3N_4. Thus, we believe that it is the porous g-C_3N_4 that has a major effect on the degradation of RhB rather than the traces of residual acids.
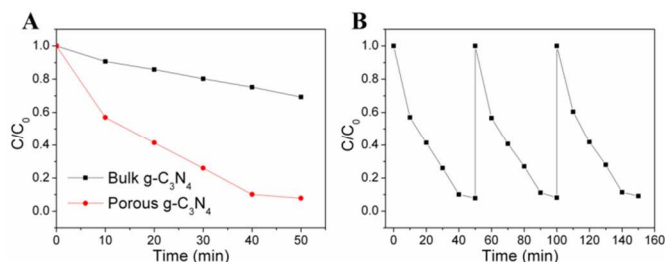

Fig. 7 (A) The photocatalytic degradation of RhB by the porous g-C_3N_4. (B) Cycling runs for the photocatalytic degradation of RhB in the presence of the porous g-C_3N_4 under visible light irradiation.

Conclusions

In summary, water-dispersible porous g-C_3N_4 with a high concentration (3 mg mL^{-1}) has been successfully prepared via a chemical oxidation method of the bulk g-C_3N_4. The porous g-C_3N_4 exhibits a large surface area and a wide band gap, which greatly improve its phtocatalytic activities under visible light. Further efforts will be made towards fabrication of self-assemblied composites of g-C_3N_4 with other materials or applications in the fields of electrocatalysts or solar cells.

Acknowledgements

Notes and references

a Department of Chemistry, Shanghai Key Laboratory of Molecular Catalysis and Innovative Materials, Fudan University, Shanghai 200433, P. R. China. E-mail: chenmeng@fudan.edu.cn

b School of Medical Instrument and Food Engineering, University of Shanghai for Science and Technology, Shanghai, 200093, P. R. China.

1. A. J. Nozik, M. C. Beard, J. M. Luther, M. Law, R. J. Ellingson and J. C. Johnson, *Chem Rev*, 2010, **110**, 6873-6890.
2. A. Thomas, A. Fischer, F. Goettmann, M. Antonietti, J.-O. Müller, R. Schlögl and J. M. Carlsson, *J. Mater. Chem.*, 2008, **18**, 4893-4908.
3. Y. Wang, X. Wang and M. Antonietti, *Angew. Chem. Int. Ed.*, 2012, **51**, 68-89.
4. J. Wirth, R. Neumann, M. Antonietti and P. Saalfrank, *Phys. Chem. Chem. Phys.*, 2014, **16**, 15917-15926.
5. X. Wang, K. Maeda, X. Chen, K. Takanabe, K. Domen, Y. Hou, X. Fu and M. Antonietti, *J. Am. Chem. Soc.*, 2009, **131**, 1680-1681.
6. S. Wang, C. Li, T. Wang, P. Zhang, A. Li and J. Gong, *J. Mater. Chem. A*, 2014, **2**, 2885-2890.
7. L. Ge, F. Zuo, J. Liu, Q. Ma, C. Wang, D. Sun, L. Bartels and P. Feng, *J. Phys. Chem. C*, 2012, **116**, 13708-13714.
8. J. Yu, K. Wang, W. Xiao and B. Cheng, *Phys. Chem. Chem. Phys.*, 2014, **16**, 11492-11501.
9. Y. Chen, J. Li, Z. Hong, B. Shen, B. Lin and B. Gao, *Phys. Chem. Chem. Phys.*, 2014, **16**, 8106-8113.
10. Q. Liu and J. Zhang, *Langmuir*, 2013, **29**, 3821-3828.
11. J. Li, B. Shen, Z. Hong, B. Lin, B. Gao and Y. Chen, *Chem. Commun.*, 2012, **48**, 12017-12019.
12. B. V. Lotsch, M. Doeblinger, J. Sehnert, L. Seyfarth, J. Senker, O. Oeckler and W. Schnick, *Chem-Eur J*, 2007, **13**, 4969-4980.
13. X. Zhang, X. Xie, H. Wang, J. Zhang, B. Pan and Y. Xie, *J. Am. Chem. Soc.*, 2013, **135**, 18-21.
14. S. Yang, Y. Gong, J. Zhang, L. Zhan, L. Ma, Z. Fang, R. Vajtai, X. Wang and P. M. Ajayan, *Adv. Mater.*, 2013, **25**, 2452-2456.
15. X. She, H. Xu, Y. Xu, J. Yan, J. Xia, L. Xu, Y. Song, Y. Jiang, Q. Zhang and H. Li, *J. Mater. Chem. A*, 2014, **2**, 2563-2570.
16. J. Xu, L. Zhang, R. Shi and Y. Zhu, *J. Mater. Chem. A*, 2013, **1**, 14766-14772.
17. F. Zhao, H. Cheng, Y. Hu, L. Song, Z. Zhang, L. Jiang and L. Qu, *Sci Rep*, 2014, **4**, 5882-5889.
18. V. Nicolosi, M. Chhowalla, M. G. Kanatzidis, M. S. Strano and J. N. Coleman, *Science*, 2013, **340**, 1226419.
19. Y. Zhang, A. Thomas, M. Antonietti and X. Wang, *J. Am. Chem. Soc.*, 2009, **131**, 50-51.
20. T. Y. Ma, Y. Tang, S. Dai and S. Z. Qiao, *Small*, 2014, **10**, 2382-2389.
21. S. C. Tsang, Y. K. Chen, P. J. F. Harris and M. L. H. Green, *Nature*, 1994, **372**, 159-162.
22. H. Hiura, T. W. Ebbesen and K. Tanigaki, *Adv. Mater.*, 1995, **7**, 275-276.
23. X. H. Chen, J. T. Xia, J. C. Peng, W. Z. Li and S. S. Xie, *Compos. Sci. Technol.*, 2000, **60**, 301-306.
24. Z. L. Liu, X. H. Lin, J. Y. Lee, W. Zhang, M. Han and L. M. Gan, *Langmuir*, 2002, **18**, 4054-4060.
25. J. Zhang, H. L. Zou, Q. Qing, Y. L. Yang, Q. W. Li, Z. F. Liu, X. Y. Guo and Z. L. Du, *J. Phys. Chem. B*, 2003, **107**, 3712-3718.
26. P. Niu, L. Zhang, G. Liu and H.-M. Cheng, *Adv. Funct. Mater.*, 2012, **22**, 4763-4770.

27. D. Tasis, N. Tagmatarchis, A. Bianco and M. Prato, *Chem Rev*, 2006, **106**, 1105-1136.

28. C. P. Murthy, *University Chemistry Volume 1*, New Age International (P) Ltd., 1995.

29. J. Tian, Q. Liu, C. Ge, Z. Xing, A. M. Asiri, A. O. Al-Youbi and X. Sun, *Nanoscale*, 2013, **5**, 8921-8924.

30. X. Wang, K. Maeda, A. Thomas, K. Takanabe, G. Xin, J. M. Carlsson, K. Domen and M. Antonietti, *Nat. Mater.*, 2009, **8**, 76-80.

31. J. Hong, X. Xia, Y. Wang and R. Xu, *J. Mater. Chem.*, 2012, **22**, 15006-15012.

32. J. Xu, H.-T. Wu, X. Wang, B. Xue, Y.-X. Li and Y. Cao, *Phys. Chem. Chem. Phys.*, 2013, **15**, 4510-4517.

33. D. Yang, A. Velamakanni, G. Bozoklu, S. Park, M. Stoller, R. D. Piner, S. Stankovich, I. Jung, D. A. Field and C. A. Ventrice Jr, *Carbon*, 2009, **47**, 145-152.

34. F. Meng, X. Zhang, B. Xu, S. Yue, H. Guo and Y. Luo, *J. Mater. Chem.*, 2011, **21**, 18537-18539.

35. M. Wu, J. M. Yan, X. n. Tang, M. Zhao and Q. Jiang, *ChemSusChem*, 2014, **7**, 2654-2658.

36. T. Y. Ma, S. Dai, M. Jaroniec and S. Z. Qiao, *Angew. Chem. Int. Ed.*, 2014, **53**, 7281-7285.

37. W. S. Hummers and R. E. Offeman, *J. Am. Chem. Soc.*, 1958, **80**, 1339-1339.

38. M. R. Hoffmann, S. T. Martin, W. Y. Choi and D. W. Bahnemann, *Chem Rev*, 1995, **95**, 69-96.

39. Y. Li, J. Zhang, Q. Wang, Y. Jin, D. Huang, Q. Cui and G. Zou, *J. Phys. Chem. B*, 2010, **114**, 9429-9434.

40. Y. Zheng, Y. Jiao, J. Chen, J. Liu, J. Liang, A. Du, W. Zhang, Z. Zhu, S. C. Smith, M. Jaroniec, G. Q. Lu and S. Z. Qiao, *J. Am. Chem. Soc.*, 2011, **133**, 20116-20119.

41. P. Larkin, *Infrared and Raman spectroscopy: principles and spectral interpretation*, Academic Press, Elsevier, 2011.

42. G. Liao, S. Chen, X. Quan, H. Yu and H. Zhao, *J. Mater. Chem.*, 2012, **22**, 2721-2726.

43. L. Qi, J. Yu and M. Jaroniec, *Phys. Chem. Chem. Phys.*, 2011, **13**, 8915-8923.

44. C. Nethravathi and M. Rajamathi, *Carbon*, 2008, **46**, 1994-1998.

45. N. Lebrun, P. Dhamelincourt, C. Focsa, B. Chazallon, J. Destombes and D. Prevost, *J. Raman Spectrosc.*, 2003, **34**, 459-464.

46. G. Möhlmann, *J. Raman Spectrosc.*, 1987, **18**, 199-203.

47. X. T. Zhang, L. Chen, T. Y. Yuan, H. Huang, Z. Y. Sui, R. Du, X. Li, Y. Lu and Q. W. Li, *Mater. Horiz.*, 2014, **1**, 232-236.

48. N. V. Medhekar, A. Ramasubramaniam, R. S. Ruoff and V. B. Shenoy, *Acs Nano*, 2010, **4**, 2300-2306.

49. Q.-F. Deng, L. Liu, X.-Z. Lin, G. Du, Y. Liu and Z.-Y. Yuan, *Chem. Eng. J.*, 2012, **203**, 63-70.

50. D. Zhou, Q. Y. Cheng, Y. Cui, T. Wang, X. X. Li and B. H. Han, *Carbon*, 2014, **66**, 592-598.

51. V. Zeleňák, M. Badaničová, D. Halamova, J. Čejka, A. Zukal, N. Murafa and G. Goerigk, *Chem. Eng. J.*, 2008, **144**, 336-342.

52. Q. Li, J. Yang, D. Feng, Z. Wu, Q. Wu, S. S. Park, C.-S. Ha and D. Zhao, *Nano Res*, 2010, **3**, 632-642.

53. Y. Xu, H. Xu, L. Wang, J. Yan, H. Li, Y. Song, L. Huang and G. Cai, *Dalton Trans.*, 2013, **42**, 7604-7613.

54. S. Chu, Y. Wang, Y. Guo, J. Feng, C. Wang, W. Luo, X. Fan and Z. Zou, *Acs Catal*, 2013, **3**, 912-919.

55. A. P. Alivisatos, *Science*, 1996, **271**, 933-937.

56. S. Ye, L.-G. Qiu, Y.-P. Yuan, Y.-J. Zhu, J. Xia and J.-F. Zhu, *J. Mater. Chem. A*, 2013, **1**, 3008-3015.

57. A. I. Hochbaum and P. Yang, *Chem Rev*, 2009, **110**, 527-546.

58. S. C. Yan, Z. S. Li and Z. G. Zou, *Langmuir*, 2009, **25**, 10397-10401.

59. G. Dong, K. Zhao and L. Zhang, *Chem. Commun.*, 2012, **48**, 6178-6180.

60. S. Kumar, T. Surendar, B. Kumar, A. Baruah and V. Shanker, *J. Phys. Chem. C*, 2013, **117**, 26135-26143.